

Leakage-Aware Bandgap Prediction on the JARVIS-DFT Dataset: A Phase-Wise Feature Analysis

Gaurav Kumar Sharma

Metallic Materials Technology

Faculty of Materials Science and Technology

TU Bergakademie Freiberg, Germany

gaurav-kumar.sharma@student.tu-freiberg.de

Abstract

In this study, we perform a systematic analysis of the JARVIS-DFT bandgap dataset and identify and remove descriptors that may inadvertently encode band-structure information, such as effective masses. This process yields a curated, leakage-controlled subset of 2,280 materials. Using this dataset, a three-phase modeling framework was implemented that incrementally incorporated basic physical descriptors, engineered features, and compositional attributes. The results show that tree-based models achieve R^2 values of approximately 0.88–0.90 across all phases, indicating that expanding the descriptor space does not substantially improve predictive accuracy when leakage is controlled. SHAP analysis consistently identified the dielectric tensor components as the dominant contributors. This work provides a curated dataset and baseline performance metrics for future leakage-aware bandgap prediction studies.

1 Introduction

The electronic bandgap is a fundamental material property that governs charge transport, optical absorption, and carrier excitation, thereby determining the suitability of materials for applications in optoelectronics, photovoltaics, and power electronics [1, 2]. Accurate bandgap prediction is therefore a central problem in materials science and device engineering. Although density functional theory (DFT) has been the dominant computational tool for estimating bandgaps, standard exchange–correlation approximations are known to systematically underestimate experimental values, and more accurate approaches, such as hybrid functionals or many-body perturbation methods, remain computationally expensive for large-scale screening.

The growing availability of high-throughput DFT repositories has enabled the use of machine learning (ML) models as efficient surrogate predictors for bandgaps. Databases such as the Joint Automated Repository for Various Integrated Simulations (JARVIS) provide large, curated datasets of electronic and structural properties, making them attractive benchmarks for

materials informatics research [3]. Leveraging such repositories, numerous studies have demonstrated that ML models can reproduce DFT-level bandgaps with reasonable accuracy while dramatically reducing the computational cost. Beyond large databases, several groups have also shown that classical ML models, when combined with careful feature selection and physically motivated descriptors, can perform well even on smaller or curated datasets [4–7].

Despite this progress, an important methodological issue has often received insufficient attention: feature leakage. Feature leakage occurs when input descriptors unintentionally encode information that is too closely related to the target property, leading to an artificially inflated model performance and misleading conclusions about the predictive capability [8]. In materials datasets, this risk arises naturally because many commonly used descriptors are derived from DFT electronic structure calculations and are therefore physically correlated with the underlying band structure [3, 9]. Such correlations do not imply data leakage by default; however, if descriptors that strongly depend on electronic eigenvalues or related quantities are included without careful screening, the resulting models may exploit hidden shortcuts rather than learning transferable structure–property relationships. Models trained under these conditions cannot be reliably used for realistic predictions or materials discovery tasks [8, 10].

In this work, we adopt a systematic strategy to address this challenge. We begin by constructing a leakage-free subset of the JARVIS bandgap database through domain-aware screening of candidate descriptors, ensuring that no input feature unfairly encodes the target bandgap. Using this curated dataset as a foundation, we introduce a three-phase modeling framework designed to isolate the impact of feature complexity on predictive performance. Phase I employs only simple, physically interpretable descriptors to establish a transparent baseline. In Phase II, engineered quantities are introduced to evaluate whether they provide genuinely independent information. Phase III incorporates composition-based descriptors generated using `Matminer` to examine how model performance evolves with a richer but potentially riskier feature space [9].

To further validate model reliability, we employ SHAP-based interpretability analysis across all three phases. This enables examination of how individual features contribute to predictions and verification of whether model behavior is governed by physically meaningful trends or by hidden correlations that may signal residual leakage [11]. Rather than treating interpretability as a post-hoc visualization tool, it is used here as an integral component of model validation.

Overall, this study aims to provide (i) a clean, leakage-free baseline dataset for bandgap prediction derived from JARVIS, (ii) a controlled, phase-wise assessment of how increasing feature complexity affects model accuracy, and (iii) physically interpretable insights into the most influential descriptors through SHAP analysis. By explicitly addressing feature leakage within a material-specific context, this study seeks to improve the reliability and interpretability of ML-based bandgap prediction models.

2 Method

2.1 Data Preprocessing and Curation

The dataset used in this study was constructed by combining two JARVIS repositories, `JARVIS-dft_3d` and `JARVIS-dft_3d_2021`. Both datasets originated from the same optB88-vdW workflow, ensuring descriptor compatibility. After merging them through their shared descriptor fields, the combined dataset contained 131,716 structures with 31 features, with `optb88vdw_bandgap` selected as the target property [3]. Duplicate compositions were resolved by retaining only the lowest-energy polymorphs, yielding 51,905 unique entries. Placeholder strings such as `na`, `[]`, `None`, and `nan` were standardized to `NaN` for consistent pre-processing. To address sparsity in several JARVIS descriptors, filtering was performed using a core set of physical quantities essential for meaningful bandgap modeling: formation energy per atom, density, number of atoms, dimensionality, space-group number, bulk and shear moduli, Poisson ratio, dielectric tensor components (`epsx`, `epsy`, `epsz`), convex-hull energy, and the bandgap. Rows missing any of these descriptors were removed, resulting in 34,969 entries.

To ensure that the dataset remained physically meaningful, a few additional filters were applied. First, entries with positive formation energies were removed, as these phases are thermodynamically unstable [11]. For Poisson’s ratio, a working range of 0.1–0.5 was used. Although classical isotropic elasticity places the lower bound of Poisson’s ratio near 0.2 [12], experimental measurements and first-principles studies have shown that several anisotropic and low-dimensional materials can exhibit stable Poisson’s ratios approaching 0.1 without violating mechanical stability [13, 14]. This slightly relaxed lower limit helped avoid rejecting such materials unnecessarily. Extremely large elastic constants were also removed, as bulk moduli above \sim 300 GPa or shear moduli above \sim 200 GPa frequently arise from numerical instabilities, convergence issues, or misreported structures in large high-throughput databases, rather than representing reliable mechanical behavior for the majority of entries [15]. Similarly, entries with anomalous dielectric tensor components were excluded to ensure a physically meaningful linear-response behavior in the dataset. Finally, materials with invalid space-group indices were discarded. After applying these checks, the dataset was reduced to 9,459 structures. To avoid mixing materials with fundamentally different dimensionalities and bonding behaviors, 0D clusters, 1D systems, and intercalated structures were removed, leaving 5,355 entries categorized as either 2D or 3D. A binary descriptor (`is_3D`) was defined accordingly. The `max_efg` descriptor, often missing in JARVIS, was reconstructed when the full EFG tensor was available by taking the maximum absolute tensor component across all the atomic sites. Entries in which reconstruction was not possible were discarded.

Leakage testing was performed using the electron and hole effective masses, since these quantities encode band-structure curvature and can therefore act as potential leakage carriers. For this diagnostic step, only materials with complete `avg_elec_mass` and `avg_hole_mass` values were retained, yielding a temporary subset of approximately 1,915 entries. Leakage signals were detected for both descriptors; therefore, they were removed entirely from the feature space. Since the modeling pipeline does not use these descriptors, the full curated set of 2,280 materials

was kept for the subsequent feature-engineering and machine-learning phases. The final dataset consisted of 2,280 physically valid materials with 23 complete descriptors and no missing values, forming the basis of a three-phase modeling framework.

2.2 Statistical Analysis for Checking Data Integrity

Several electronic and optical features, such as effective masses, SLME, spillage, and electronic dielectric components, were removed because their limited availability would have eliminated nearly 50–60% of the 2,280 entries. Features such as `encut` and `kpoint_length_unit` were also excluded since they reflect DFT numerical settings rather than intrinsic material properties and are known sources of leakage.

To maintain physical relevance, only descriptors that were complete and scientifically meaningful were retained. After reducing the dataset from 51,905 unique entries to 2,280, a statistical integrity check was carried out to ensure that the curated dataset remained reliable and representative.

The assessment focused on whether (i) key property distributions remained meaningful, (ii) the chemical space was preserved, and (iii) the core descriptor ranges remained physically reasonable. Overall, these checks confirmed that strict filtering did not introduce unwanted bias or remove the essential variability required for machine learning models.

2.2.1 Distribution Consistency and Chemical-Space Coverage

A Kolmogorov–Smirnov (K–S) test comparing the bandgap distributions before and after filtering showed a significant shift ($D = 0.0562$, $p < 0.001$), which is expected after removing incomplete or unstable entries. Even so, the overall shape of the distribution remained similar, and the curated dataset is now dominated by physically well-behaved compounds. PCA on 12 complete descriptors further showed that the top five components captured 77.4% of the variance of the raw subset, and nine components were required to reach 95%. This indicates that, despite the large reduction in size, the essential chemical and structural diversity was reasonably preserved.

2.2.2 Physical-Property Range Preservation

To evaluate whether essential physical variability was maintained, the ranges of three fundamental descriptors were compared between the raw and curated datasets in Table 1.

Table 1: Fraction of physical-property ranges preserved after dataset curation, comparing the raw and leakage-controlled JARVIS-DFT subsets.

Property	Range Preserved (%)
Bandgap	38.5
Density	91.5
Formation energy per atom	44.8

Density shows excellent retention, while the narrowing of the bandgap and formation energy ranges reflects the removal of unstable or incomplete entries, an expected trade-off when restricting the dataset to physically meaningful values.

2.2.3 Summary and Interpretation

The combined results from the K–S test, PCA, and property range comparison show that the final dataset remains statistically robust and chemically diverse, even after major size reduction. Although some rare chemistries and extreme values were lost, which is unavoidable when enforcing physical consistency and removing leakage-prone descriptors, the curated dataset retains the variability needed for developing reliable, leakage-free machine-learning models and is scientifically suitable for further predictive work.

2.3 Data Leakage Detection and Mitigation Framework

Machine learning models are particularly vulnerable to data leakage, which occurs when the features in the input dataset inadvertently encode the target property. This can result in phantom progress, where benchmark metrics improve without corresponding gains in real-world generalization, thereby undermining scientific reliability in material machine learning [10]. At the feature level, such misleading performance gains often arise when proxy variables encode the target outcome, producing artificially inflated accuracy without genuine predictive insights [8].

In materials datasets, this risk is amplified by the use of computationally derived descriptors and metadata, which can introduce strong but unintended correlations if not carefully screened. To address these challenges, this study adopts a systematic leakage detection and mitigation framework. In addition, redundancy-aware feature-selection strategies, such as the relevance redundancy optimization employed in the MODNet framework, are essential for improving robustness and generalization in data-limited materials science applications [6].

A three-stage protocol was implemented to detect and mitigate the target leakage.

2.3.1 Feature Risk Categorization

The features were categorized based on their physical origin and potential to encode bandgap information to create a shortlist for formal leakage testing (Table 2).

Table 2: Categorization of descriptors based on leakage risk, physical origin, and potential to encode bandgap-related information.

Risk Category	Descriptors	Rationale & Origin
High-Risk	<code>avg_elec_mass</code> , <code>avg_hole_mass</code>	Derived from band-structure curvature (DFT post-processing); high potential to encode target.
Medium-Risk	<code>epsx</code> , <code>epsy</code> , <code>epsz</code>	Dielectric tensor from DFPT (independent perturbation); physical correlation without mathematical encoding of bandgap.
Low-Risk	<code>formation_energy_per_atom</code> , <code>density</code> , <code>nat</code> , <code>bulk_modulus_kv</code> , <code>shear_modulus_gv</code> , <code>poisson</code> , <code>ehull</code> , <code>max_efg</code> , <code>spg_number</code> , <code>is_3D</code> , <code>dimensionality</code>	Intrinsic structural and thermodynamic quantities; no electronic band-structure information.

2.3.2 Baseline Performance Estimation

A leakage-free performance baseline was established using only low- and medium-risk descriptors. Random Forest and XGBoost models were trained on this feature set, deliberately excluding the high-risk `avg_elec_mass` and `avg_hole_mass` descriptors.

2.3.3 Incremental Feature-Impact Analysis

Each high-risk feature was individually added to the baseline set, and the models were retrained. The evaluation included three configurations: baseline, baseline + `avg_elec_mass`, and baseline + `avg_hole_mass`. A feature was flagged as a source of leakage if its inclusion caused an unexpected and physically unrealistic performance improvement. The addition of either effective mass caused R^2 to surge to 0.90–0.93 and MAE to fall to approximately 0.05 eV, markedly exceeding the typical DFT bandgap prediction benchmarks and confirming both as leakage features.

2.4 Machine Learning

2.4.1 Hierarchical Feature Engineering Framework

To study how different types of descriptors affect the bandgap predictions, the feature set was constructed in three stages. The first stage included only fundamental physical descriptors. In the second stage, a group of engineered features derived from the basic physical descriptors was added to the model. In the final stage, composition-based descriptors that capture broader chemical trends were introduced. Constructing the feature space in this hierarchical manner enabled a clearer assessment of how the model behavior evolved as additional information was incorporated, rather than mixing all descriptor types from the outset.

Phase I: Fundamental Physical Descriptors Phase I established a baseline model using 12 intrinsic physical properties directly extracted from the curated JARVIS-DFT dataset. These descriptors capture core thermodynamic, mechanical, electronic, and structural characteristics known to influence bandgap behavior.

- **Thermodynamic:** `formation_energy_per_atom`, `ehull`
- **Mechanical:** `bulk_modulus_kv`, `shear_modulus_gv`, `poisson`
- **Electronic:** dielectric tensor components (`epsx`, `epsy`, `epsz`)
- **Structural:** `density`, `nat`, `is_3D`
- **Local electronic environment:** `max_efg`

This phase forms the benchmark for the later stages. Notably, in these experiments, this set already captured most of the model’s predictive ability. Consequently, the feature additions in Phases II and III did not lead to noticeable improvements over this baseline. This makes Phase I a useful point of comparison for evaluating whether more complex descriptors provide any real benefit.

Phase II: Engineered Physical Descriptors Phase II expands the feature set by adding a set of engineered descriptors that capture relationships that are not directly available from the raw Phase I features. These descriptors were derived through simple analytical transformations of the basic physical properties, with a small stabilizing constant ($\varepsilon = 1 \times 10^{-12}$) applied when needed to avoid numerical issues. The engineered features used in this phase were as follows:

- **Dielectric response:** `dielectric_mean`, `dielectric_anisotropy`
- **Ductility indicator:** `pugh_ratio` (gv/kv)
- **Elastic wave and stiffness proxies:** `v_t_proxy`, `v_l_proxy`, `specific_stiffness`
- **Coupling descriptor:** `stability_stiffness_ratio`

The goal of this phase was to determine whether introducing these physically motivated combinations improved the model before adding the chemistry-driven descriptors used in Phase III.

Phase III: Compositional and Orbital Descriptors Phase III introduces compositional and orbital features by adding them directly to the fundamental descriptors from Phase I. This isolates the impact of chemical information from the engineered physical transformations in Phase II. Here, the goal is to combine physical, chemical, and orbital features into the input feature set to evaluate their impact on prediction performance. Extraction of features such as element properties, valence orbital information, and ionic properties was performed using the `Matminer` toolkit [9] through the composition of the materials in the data.

A total of 132 MagpieData features were added to the base data. In addition to the Magpie atomic features, orbital and ionic property features were also extracted. In addition, 11 engineered chemical and structural descriptors were generated, as shown in Table 3.

Table 3: Engineered chemical, orbital, and structural descriptors introduced in Phase III, including their mathematical definitions, physical interpretations, and value ranges within the dataset.

Descriptor Name	Mathematical Definition	Physical Meaning	Range (Dataset)
Bond Polarity Index	$(\Delta\chi)^2$	Measures electronegativity contrast; higher values indicate increased ionic character	0.00–8.29
Atomic Size Homogeneity	$1 / (1 + (r_{\max} - r_{\min}) / r_{\text{mean}})$	Uniformity of atomic radii; 1 = perfectly uniform	0.32–1.00
Relative Electronegativity Range	$(\chi_{\max} - \chi_{\min}) / \chi_{\text{mean}}$	Normalized spread in electronegativity among constituent atoms	0.00–1.34
Radius Mismatch	$(r_{\max} - r_{\min}) / r_{\text{mean}}$	Degree of mismatch between smallest and largest atomic sizes	0.00–2.15
Atomic Size Uniformity	$r_{\text{mean}} / r_{\max}$	Ratio capturing size compactness relative to the largest atom	0.38–1.00
Radius Variance	$(r_{\text{std}})^2$	Statistical variance of covalent radii	0.00–7056.00
Pauling Ionicity Proxy	$1 - \exp[-0.25 \cdot (\Delta\chi)^2]$	Pauling's ionicity measure capturing ionic contribution to bonding	0.00–0.87
d-Hybridization Trend	f_d	Extent of d-orbital participation in bonding	0.00–0.97
p–d Orbital Interaction Index	$f_p \times f_d$	Strength of hybridization between p- and d-orbitals	0.00–0.175
s–p Promotion Index (clipped)	f_s / f_p	Relative contribution of s vs. p valence electrons	0.38–10.00
Transition-Metal Electron Index	$\text{mean}(f_d)$	Characterizes transition-metal content in the composition	0.00–0.97

After the addition of the engineered and Magpie features, the total number of features increased to 170. Variance and correlation filtering were applied to identify redundant inputs. A variance threshold of 0.001 was used, which removed one near-constant feature. This was followed by correlation filtering with a cutoff value of 0.95. A conservative threshold was intentionally adopted to avoid removing chemically meaningful descriptors; this step eliminated 46 highly correlated features from the dataset. In total, 47 features were removed, resulting in a cleaned dataset with 123 features. Also, during variance and correlation filtering, one dielectric tensor component was removed due to strong collinearity with the remaining components, reflecting statistical redundancy rather than physical exclusion.

After this preprocessing, feature selection was performed using the XGBoost-based importance ranking. The models were then trained using feature subsets ranging from 10 to 123 features, with the subset size increasing in steps of five to determine the optimal number of features for achieving the highest prediction accuracy.

2.5 Machine Learning Modeling

Three training permutations were performed for each machine-learning model to test the robustness of the model predictions. Five different algorithms were used: Ridge Regression, SVR, Random Forest, XGBoost, and CatBoost. These models were chosen because they cover a spectrum from linear to kernel-based to tree-based learning methods. This helps in understanding how the material datasets behave across different types of algorithms.

2.5.1 Model Architectures and Hyperparameter Optimization

Ridge Regression was used as the linear baseline. It was implemented through a simple `StandardScaler-Ridge` pipeline, and the regularization strength was kept fixed at $\alpha = 1.0$ for all experiments. For the nonlinear baseline, Support Vector Regression (SVR) was used with an RBF kernel.

The main SVR hyperparameters were tuned using a 5-fold `GridSearchCV`. The following search space was employed:

- C : 1, 10, 100, 500
- ε : 0.01, 0.05, 0.1
- γ : `scale`, 0.1, 0.5, 1

These two models were also tested alongside three tree-based methods: Random Forest, XGBoost, and CatBoost. These algorithms are well known for handling nonlinear patterns and feature interactions that frequently occur in materials datasets. Table 4 provides the precise values of the hyperparameters and settings of the tree models.

Three tree-based models were included because they can capture nonlinear relationships and feature interactions more effectively than linear or kernel methods [16]. The specific hyperparameters and model settings used for these tree models are presented in Table 4.

Table 4: Hyperparameter configurations used for tree-based machine-learning models (Random Forest, XGBoost, and CatBoost) under conservative, balanced, and aggressive settings.

Model	Configuration	Hyperparameters
Random Forest	Conservative	<code>n_estimators</code> = 500, <code>max_depth</code> = 13, <code>min_samples_leaf</code> = 5
	Balanced	<code>n_estimators</code> = 600, <code>max_depth</code> = None
	Aggressive	<code>n_estimators</code> = 700, <code>max_depth</code> = None, <code>min_samples_leaf</code> = 1
XGBoost	Conservative	<code>n_estimators</code> = 500, <code>learning_rate</code> = 0.05, <code>max_depth</code> = 6

Continued on next page

Model	Configuration	Hyperparameters
CatBoost	Balanced	<code>n_estimators = 600, learning_rate = 0.10,</code> <code>max_depth = 8</code>
	Aggressive	<code>n_estimators = 700, learning_rate = 0.30,</code> <code>max_depth = 6</code>
	Conservative	<code>iterations = 1000, learning_rate = 0.01,</code> <code>depth = 6, l2_leaf_reg = 5</code>
	Balanced	<code>iterations = 3000, learning_rate = 0.05,</code> <code>depth = 10, l2_leaf_reg = 1</code>
	Aggressive	<code>iterations = 2000, learning_rate = 0.03,</code> <code>depth = 8, l2_leaf_reg = 3</code>

2.5.2 Training and Evaluation Protocol

The models were trained and tested across the three phases using a single, consistently defined train–test split. A 4:1 ratio was used for training and testing, which is common practice in materials informatics. Keeping the split fixed across all phases made it possible to directly compare how the predictions changed when new feature sets were introduced. The hyperparameters were also kept constant within each model type to allow a fair phase-wise comparison. For Ridge and Support Vector Regression (SVR), feature scaling was performed using a standard scaler.

To prevent data leakage, the scaler was fitted only to the training data and then applied to the test data. The tree-based models were trained on raw, unscaled features. A random seed of 42 was used for all the randomization steps to maintain reproducibility. The evaluation settings and metrics remained the same for all phases and models to ensure valid comparison. Model evaluation was performed in two parts:

- **Numerical Performance Evaluation:** The following metrics were used to quantify model performance.
 - **R^2 score:** Measures how closely the predicted bandgap values match the actual bandgaps.
 - **Mean Absolute Error (MAE):** Represents the average absolute difference between predicted and true bandgaps (in eV).
 - **Mean Squared Error (MSE):** Similar to MAE but applies a squared penalty to larger errors, making the metric more sensitive to large deviations.

Together, these three metrics provide a comprehensive view of each model’s accuracy and error characteristics.

- **SHAP-Based Model Interpretation:** Shapley additive explanation (SHAP) analysis [17] was used to interpret the model outputs and understand how individual features contribute to the bandgap prediction. This analysis was applied only to the tree-based

models in each phase, as the SHAP values for tree ensembles are well-established and more reliable. The SHAP study offers phase-wise insights into which features have the greatest influence on the predictions.

3 Results

3.1 Effect of Effective-Mass Descriptors on Model Performance

Including the descriptors `avg_elec_mass` and `avg_hole_mass` led to a substantial increase in the model accuracy. The R^2 score increased from 0.727–0.806 to 0.902–0.931, while the MAE decreased from approximately 0.10 eV to 0.055 eV and the MSE decreased from 0.08–0.10 to 0.028–0.039. The corresponding performance comparison is presented in Figure 1.

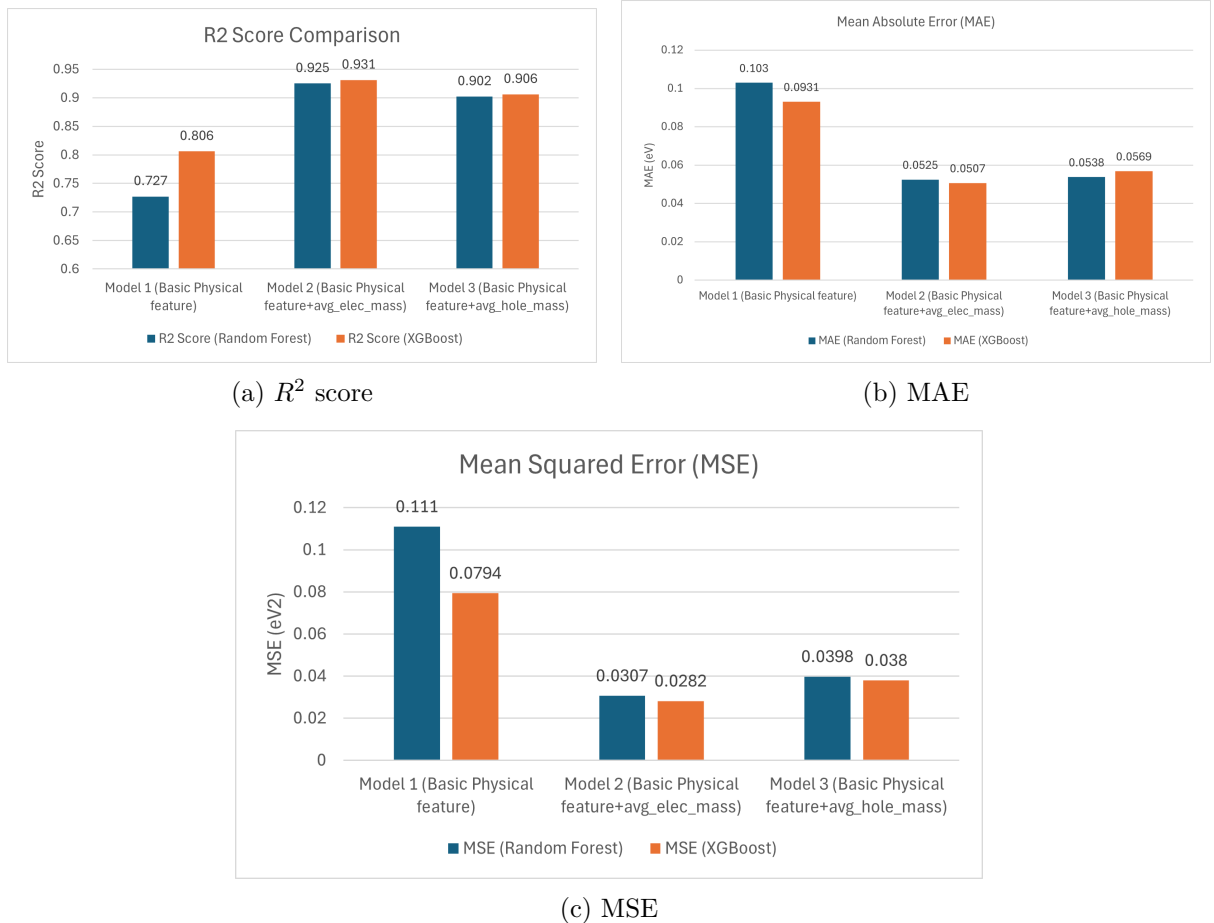


Figure 1: Effect of effective-mass descriptors on model performance. (a) R^2 score, (b) mean absolute error (MAE), and (c) mean squared error (MSE) for models trained with and without effective-mass features.

3.2 Phase-wise Model Performance Across Feature Sets

The three-phase framework for assessing model prediction accuracy with variations in the input features is outlined here. In each phase, five models were trained to evaluate the performance

of the feature set. Phase-wise modeling also allows a clear understanding of how feature engineering affects the prediction when the same input features are used and how the incorporation of Matminer’s atomic features together with engineered chemical and structural descriptors influences bandgap prediction in materials.

Table 5: Phase-wise model performance for bandgap prediction. Reported values correspond to the best configuration among the three hyperparameter settings for each model.

Model	Phase	R^2	MAE (eV)	MSE (eV ²)
Ridge	I: Fundamental	0.458	0.497	0.615
	II: Engineered	0.460	0.490	0.613
	III: Compositional (Full features)	0.599	0.466	0.455
SVR	I: Fundamental	0.751	0.236	0.283
	II: Engineered	0.713	0.261	0.325
	III: Compositional (Full features)	0.755	0.252	0.278
Random Forest	I: Fundamental	0.899	0.135	0.115
	II: Engineered	0.904	0.129	0.106
	III: Compositional (Top 110 features)	0.880	0.134	0.137
XGBoost	I: Fundamental	0.894	0.131	0.119
	II: Engineered	0.889	0.131	0.126
	III: Compositional (Top 110 features)	0.893	0.133	0.121
CatBoost	I: Fundamental	0.887	0.135	0.127
	II: Engineered	0.883	0.150	0.133
	III: Compositional (Top 110 features)	0.896	0.137	0.117

3.3 Phase-wise Analysis of Model Performance

The three-phase framework for assessing model prediction accuracy with variations in the input features is outlined here. In each phase, five models were trained to evaluate the performance of the feature set. Phase-wise modeling also allows a clear understanding of how feature engineering affects the prediction when the same input features are used and how the incorporation of Matminer’s atomic features together with engineered chemical and structural descriptors influences bandgap prediction in materials. Table 5 presents the model-wise results (best of the three hyperparameter settings) for the predicted bandgap values for the three phases.

Phase I: Baseline Physical Descriptors Provide Foundational Predictive Performance

Phase I involved predictions using a selected baseline feature set comprising only physically measurable descriptors. The cleaned input data were sourced from the JARVIS dataset, and five machine learning models were trained on this uniform feature set. The observed results align well with the known behaviors of these algorithms. As expected, Ridge Regression exhibited the weakest performance, failing to achieve an R^2 above 0.50, indicating that linear models underfit

the underlying relationships. Support Vector Regression (SVR) displayed moderate predictive capability, whereas tree-based models performed strongly, with XGBoost achieving the highest accuracy, as shown in Table 5.

Phase II: Engineered Physical Descriptors Added to the Baseline Feature Set

In Phase II, the baseline physical descriptors were supplemented with a set of engineered features derived from them, creating a slightly larger but still physics-motivated input space. The models were retrained using the same train–test split as in Phase I to ensure a fair comparison.

Overall, the expanded feature set did not lead to any noticeable improvements. Ridge Regression shows only a marginal change (from $R^2 = 0.458$ to 0.460), while SVR actually performs slightly worse. The tree-based models, Random Forest, XGBoost, and CatBoost, exhibited essentially unchanged performance between Phase I and Phase II, with differences in R^2 limited to 0.003 – 0.01 . These changes are numerically negligible relative to the overall model accuracy and indicate that the addition of engineered physical descriptors does not provide any meaningful performance gain for the ensemble-based methods. Taken together, the Phase II results indicate that adding engineered physical descriptors to the baseline feature set does not materially enhance the predictive performance of any model. The overall trend remains essentially identical to that observed in Phase I.

Phase III: Matminer Features with Baseline Descriptors

In Phase III, the feature set was expanded quite a bit by adding a larger group of Matminer descriptors on top of the original physical features. These include several compositional, chemical, and orbital features, along with a handful of Matminer-engineered features already listed in the Methods section. No engineered physical descriptors from Phase II were used here.

Before training the main models, a small feature sweep was performed using a simple Random Forest model. The goal was just to check how the accuracy changes as the number of features increases. Feature counts from 10 up to 123 were tested in steps of five. The trend peaked around 110 features, as shown in Figure 2, so that number was taken forward for the tree-based models in this phase. With those 110 features, the ensemble models were retrained. Random Forest reached an R^2 of 0.880 with an MAE of 0.134 eV and an MSE of 0.137 eV 2 . XGBoost performed slightly better, recording $R^2 = 0.893$, MAE = 0.133 eV, and MSE = 0.121 eV 2 . Among all the models tested in this phase, CatBoost yielded the highest score, with $R^2 = 0.896$, MAE = 0.137 eV, and MSE = 0.117 eV 2 .

Ridge Regression and SVR were trained using the full set of 123 features. The ridge improved compared to the previous phases and reached $R^2 = 0.599$, with an MAE of 0.466 eV and an MSE of 0.455 eV 2 . SVR stayed close to its earlier performance, giving $R^2 = 0.755$, MAE = 0.252 eV, and MSE = 0.278 eV 2 .

An error-distribution plot (Figure 3) was generated for CatBoost, as it was the best-performing model. The mean prediction error was 0.029 eV, and the standard deviation was approximately

0.3416 eV. Most predictions were close to zero, and only a few noticeable outliers appeared in the distribution.

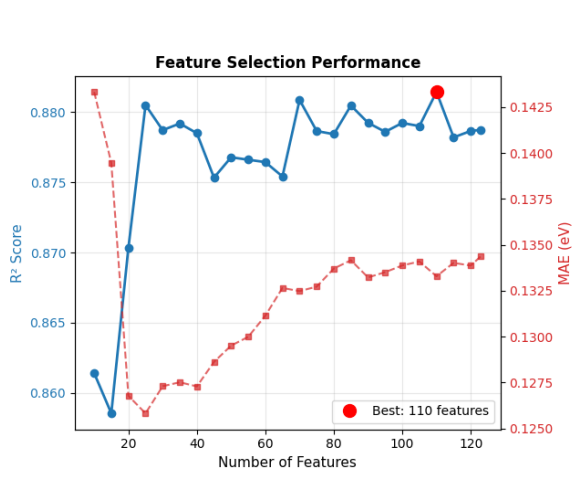


Figure 2: Model performance as a function of the number of input features used to identify the optimal feature subset size.

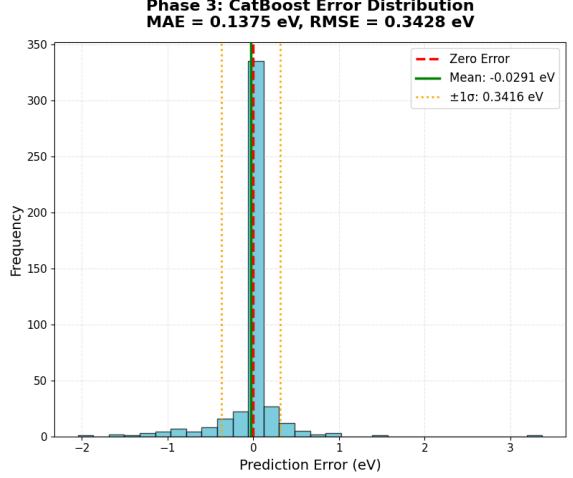
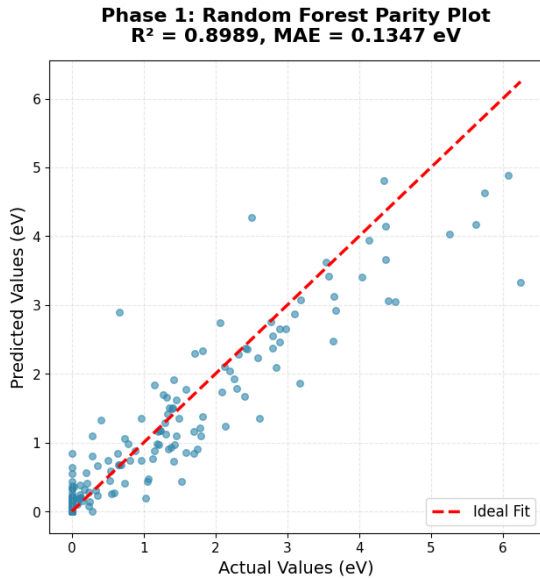


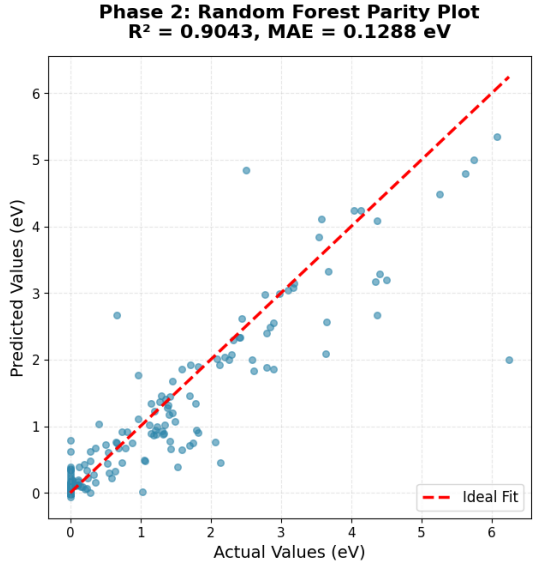
Figure 3: Error distribution for the CatBoost model trained using the Phase III feature set, showing the distribution of prediction residuals.

3.4 Phase-Wise Parity Plot Comparison

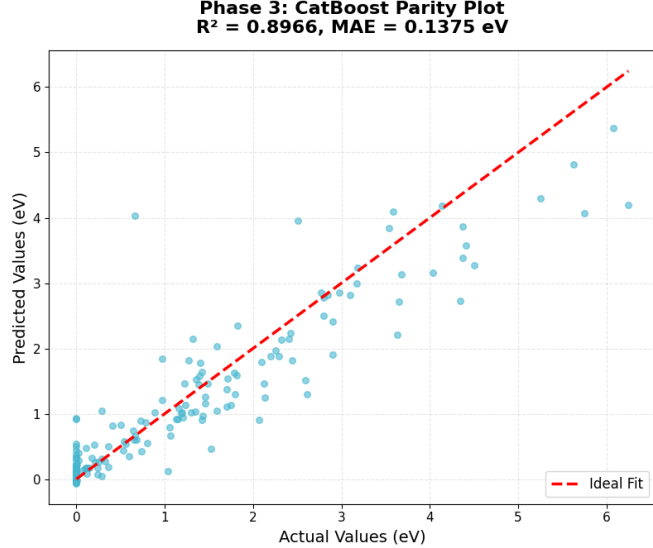
Figure 5 shows the parity plots of the best-performing models from each phase. The three plots exhibit a very similar overall pattern: the predicted values align closely with the ideal-fit line, and the spread of points remains nearly unchanged across the phases. Despite the progressive increase in feature dimensionality, the general prediction behavior remained consistent, with no substantial shift in accuracy or scatter characteristics from Phase I to Phase III.



(a) Phase I



(b) Phase II

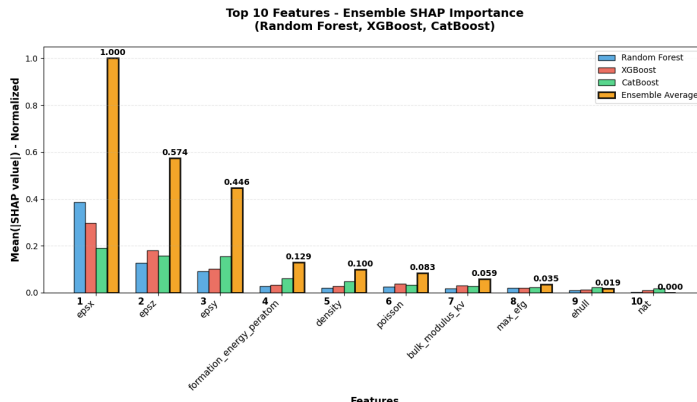


(a) Phase III

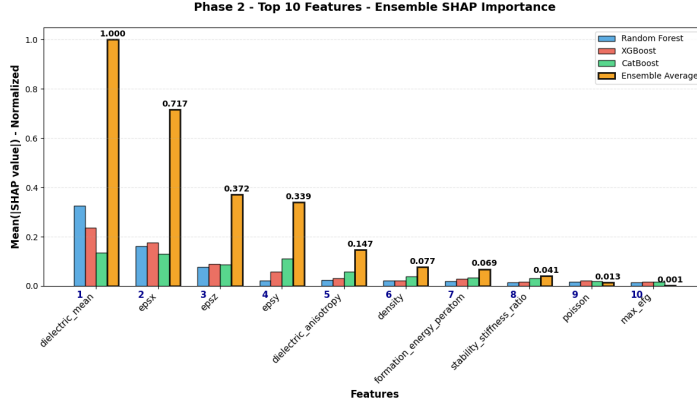
Figure 5: Phase-wise parity plots for the best-performing models in Phase I, Phase II, and Phase III, comparing predicted and reference bandgap values. The predicted values align closely with the ideal-fit line across all phases, indicating consistent predictive behavior despite increasing feature complexity.

3.5 Feature Importance Across the Three-Phase Modeling Framework (SHAP Analysis)

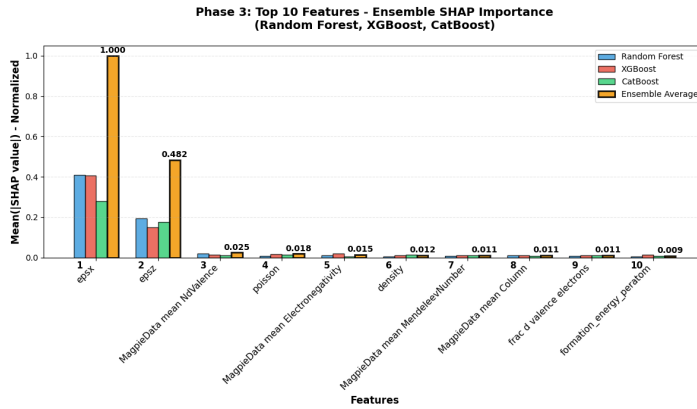
Across all three phases, the SHAP analysis (Figure 6) shows a consistent pattern: the dielectric tensor components remain the dominant predictors of the bandgap, while the remaining features mainly provide secondary support to the model. In Phase I, the three principal dielectric components (epsx, epsy, and epsz) clearly dominated the feature rankings. In Phase II, the engineered dielectric descriptor introduced in this phase emerged as the strongest contributor, with the individual dielectric tensor components following closely behind. In Phase III, where Matminer-derived compositional and chemical attributes are added, the dielectric features again appear at the top of the importance list, whereas the Magpie descriptors contribute primarily as supporting features rather than leading ones. This phase-wise consistency highlights that the dielectric response of a material plays a central role in driving the predictive performance of the models, regardless of how the overall feature space evolves.



(a) Phase I: Baseline physical descriptors.



(b) Phase II: Baseline physical descriptors + Engineered physical descriptors



(c) Phase III: Fundamental physical descriptors + Compositional and Matminer descriptors

Figure 6: SHAP-based feature importance analysis for the best-performing models across the three modeling phases. (a) Phase I: Baseline physical descriptors. (b) Phase II: Baseline physical descriptors with engineered features. (c) Phase III: Baseline physical descriptors with compositional and Matminer features. Dielectric tensor components consistently dominate the feature rankings, while the added compositional and Matminer-derived descriptors contribute primarily as secondary features.

4 Discussion

4.1 Importance of Leakage-Free Modeling and Comparison with Prior Work

The performance comparison in Figure 1 highlights the strong influence of effective-mass descriptors on the predictive accuracy of bandgap regression models. When the models were trained using only the physical descriptors, the accuracy remained within a stable and physically reasonable range. However, introducing the features *avg_elec_mass* and *avg_hole_mass* produced an immediate and disproportionate improvement across all evaluation metrics, with R^2 increasing to above 0.90 and MAE and MSE decreasing by approximately a factor of two. Such abrupt changes suggest that these descriptors introduce target leakage into the modeling

pipeline.

The underlying reason for this behavior can be traced to the physics of band-structure calculations. In semiconductor theory, the electron and hole effective masses are defined through the curvature of the energy bands near the extrema,

$$m^* = \hbar^2 \left(\frac{d^2 E}{dk^2} \right)^{-1} \quad (1)$$

This relationship is well established in the literature [1, 18]. The JARVIS-DFT workflow reports these quantities as part of the band-structure outputs [3]. Because the bandgap and effective masses originate from the same underlying electronic structure calculations, the effective mass descriptors inherently encode information related to the target property. Their presence therefore enables the models to exploit correlations that arise directly from the band-structure itself, rather than inferring the bandgap purely from independent physical descriptors. While previous studies have highlighted the risk of unintended target proxies and feature-related pitfalls in materials machine learning workflows [7], few studies have explicitly quantified how band-structure-derived descriptors can distort the predictive performance in bandgap regression. The present analysis directly contrasts the leakage-free results with those obtained using effective-mass terms, making the magnitude of their impact transparent. This comparison underscores the necessity of excluding such descriptors when constructing generalizable bandgap-prediction models. By removing the effective-mass features from all phases of the modeling, this study established a physically grounded and leakage-controlled baseline for evaluating the machine learning performance on the JARVIS-DFT dataset.

4.2 Hierarchical Feature Engineering and Evidence of Saturation in Predictive Accuracy

The three-phase feature expansion framework was designed to examine whether progressively richer descriptors yielded measurable improvements in bandgap prediction. However, the results show that the R^2 values remain confined to a narrow band of approximately 0.88–0.90 across all phases, suggesting that the predictive capacity of leakage-free features in the JARVIS-DFT dataset saturates early. The models did not exhibit the sequential accuracy gains typically expected when meaningful new information was added to the feature space.

In Phase I, the classical models trained on fundamental physical descriptors already achieved strong predictive performance. These descriptors include the dielectric tensor components, elastic moduli, Poisson’s ratio, formation energy per atom, and material dimensionality. SHAP analysis consistently identifies the dielectric tensor components as the dominant contributors, reflecting their strong influence on dielectric screening and band-edge behavior, two physical factors closely tied to a material’s bandgap.

Phase II introduces engineered descriptors designed to capture more nuanced physical phenomena, such as dielectric anisotropy, mean dielectric response, Pugh ratio, and stability–stiffness relationships. Although these features enrich the physical interpretability of the model, their

contribution to the accuracy remains modest. The small variations in R^2 , MAE, and MSE were numerically minor relative to the overall model accuracy, indicating that these engineered descriptors provided incremental rather than transformative information relative to the Phase I feature set.

Phase III incorporates a much broader set of Matminer-derived chemical and orbital descriptors, substantially expanding the dimensionality of descriptor space. Despite this increase, the overall performance remained comparable to the earlier phases, again centered around $R^2 \approx 0.89$. The SHAP rankings show that the dielectric tensor components continue to dominate, whereas the Matminer descriptors primarily act as supporting features. This apparent saturation likely reflects the limited information content of optB88vdW-level descriptors with respect to bandgap variability, rather than a fundamental limitation of machine-learning models themselves. These findings suggest that simply increasing the number of descriptors does not necessarily enhance the predictive performance; even with the addition of an extensive suite of Matminer features, the model does not exhibit appreciable gains in accuracy.

Taken together, these observations point to feature-information saturation within the JARVIS-DFT dataset for classical machine-learning models. Expanding the descriptor richness from fundamental physical descriptors to engineered physical features and finally to comprehensive Matminer compositional descriptors did not produce successive improvements in predictive capability. Instead, the models converged to a stable accuracy ceiling governed primarily by the dielectric properties. It should also be noted that this conclusion applies specifically to the classical ML models examined here; deep learning architectures were not evaluated and may display different sensitivities to high-dimensional feature spaces or latent representation learning.

4.3 SHAP Interpretation Across Phases: Consistent Dominance of Dielectric Features

SHAP analysis provides a unifying perspective on how the models predict across all three phases. In Phase I, the dielectric tensor components emerged as the most influential descriptors for every tree-based model, far outweighing the mechanical or structural features. This behavior is physically intuitive because the dielectric response is closely connected to how a material screens electric fields and reflects the electronic polarizability near the band edges, both of which correlate strongly with bandgap trends across the chemical space.

Phase II maintained this pattern. Although the introduction of engineered descriptors improves interpretability, it does not alter the hierarchy of the feature importance. The engineered dielectric descriptors become more prominent in this phase, but they reinforce the same underlying signal captured by the raw dielectric components rather than replacing it.

Even in Phase III, where the descriptor space expands substantially through the inclusion of Matminer chemical and orbital features, the dielectric tensor components remain the dominant contributors. The compositional and chemical features play meaningful but clearly secondary roles, supporting rather than redefining the predictive structure of the models. The SHAP rankings show that the tree-based models consistently rely on dielectric behavior as the pri-

mary source of information, with mechanical and chemical descriptors providing additional refinements.

Taken together, the SHAP analysis highlights a robust and phase-independent pattern: the dielectric properties govern the predictive performance across all feature sets, whereas the chemical, structural, and mechanical descriptors function mainly as complementary inputs. This reinforces that the models are learning physically grounded relationships rather than shortcut correlations. It also supports the broader conclusion that the JARVIS bandgap dataset contains a strong dominant signal—dielectric screening—that classical models capture effectively even when additional descriptors are introduced.

4.4 Limitations and Future Work

This study has several limitations that also point toward clear directions for future development.

First, the dataset size decreased substantially during the curation stage. Although strict filtering ensured physical consistency, it also removed many chemically complex and compositionally diverse materials. The resulting dataset was more homogeneous and may have limited the model’s exposure to rare chemistries, thereby constraining the generalizability of the predictions.

Second, the models were trained exclusively on optB88vdW bandgaps computed within the JARVIS-DFT workflow. As a result, the predicted values inherit the systematic behavior and biases of this specific functional and do not directly translate to higher-fidelity hybrid-functional (e.g., HSE06) or experimental bandgaps. The lack of high-fidelity electronic-structure descriptors, many of which are lost during the leakage removal process, further limits the richness of the predictive space.

Third, this study relies solely on classical machine-learning models. While these methods perform well on moderately sized datasets, they may be insufficient to capture broader, highly nonlinear electronic-structure correlations that could emerge from larger, more heterogeneous datasets or from deep-learning architectures specifically designed to learn long-range chemical and structural patterns.

These limitations suggest several concrete pathways for future research. (1) Aggregating data from multiple repositories, such as the Materials Project, OQMD, and AFLOW, would expand the dataset, restore chemical diversity, and incorporate bandgaps computed using a range of exchange–correlation functionals. (2) Once larger datasets are available, deep learning models can be developed to learn more expressive latent representations that classical models may not capture. (3) Transfer learning offers a promising strategy: a deep model can first be trained on large, low-fidelity datasets (e.g., optB88vdW) and subsequently fine-tuned on smaller sets of high-fidelity HSE or carefully curated experimental bandgaps. This approach may help bridge the gap between DFT-level predictions and experimental reality.

Collectively, these extensions would improve the fidelity, generalizability, and practical applicability of leakage-free bandgap-prediction models.

5 Conclusion

In this study, a leakage-free machine-learning framework was developed for predicting bandgaps using a physically curated subset of the JARVIS-DFT dataset. After removing leakage-prone descriptors and enforcing strict data-cleaning criteria, the models were evaluated across three progressively enriched feature sets. Despite expanding the descriptor space from fundamental physical features to engineered descriptors and finally to Matminer-derived descriptors, including some engineered attributes, the predictive accuracy of classical ML models remained essentially unchanged, saturating around $R^2 \approx 0.88\text{--}0.90$. SHAP analysis revealed a consistent phase-independent behavior: the dielectric tensor components dominated the predictions, whereas the chemical and mechanical features acted as secondary contributors.

These findings show that for leakage-free bandgap regression on the JARVIS-DFT data, adding more descriptors does not necessarily enhance model performance once the leakage is controlled. Instead, a small set of physically meaningful features governs the predictability, and classical models rapidly reach an accuracy ceiling. This ceiling should be interpreted as a diagnostic bound imposed by the available leakage-free descriptors in the JARVIS-DFT dataset, rather than as a fundamental upper limit on bandgap prediction accuracy. This highlights the importance of careful data curation, leakage detection, and interpretable machine learning in the field of materials informatics. This work is intended as a controlled diagnostic study of leakage and feature saturation in classical ML models on JARVIS-DFT bandgap data, rather than as a comprehensive benchmark across architectures or datasets. Future work involving larger multi-source datasets, deep-learning architectures, and transfer-learning strategies may help surpass the saturation observed in this study and move closer to experimentally aligned bandgap predictions.

References

- [1] S. M. Sze and K. K. Ng. *Physics of Semiconductor Devices*. Wiley, Hoboken, NJ, 3 edition, 2007.
- [2] Mark Fox. *Optical Properties of Solids*. Oxford University Press, Oxford, 2001.
- [3] Kamal Choudhary, Kevin F. Garrity, Brian DeCost, Francesca Tavazza, et al. The joint automated repository for various integrated simulations (jarvis) for data-driven materials design. *npj Computational Materials*, 6:173, 2020.
- [4] R. Yuan et al. Band gap prediction for inorganic materials using machine learning. *Materials Today Communications*, 35:105838, 2023.
- [5] S. Ghosh and J. Chowdhury. Predicting band gaps of abn_3 perovskites. *RSC Advances*, 14:6385–6397, 2024.
- [6] P.-P. De Breuck, G. Hautier, and G.-M. Rignanese. Materials property prediction for limited datasets enabled by feature selection and joint learning with modnet. *npj Computational Materials*, 7:83, 2021.

- [7] A. Y.-T. Wang, S. K. Kauwe, R. J. Murdock, and T. D. Sparks. Machine learning for materials scientists: An introductory guide toward best practices. *Chemistry of Materials*, 32:4954–4965, 2020.
- [8] S. Kapoor and A. Narayanan. Leakage and the reproducibility crisis in machine-learning-based science. *Patterns*, 4:100804, 2023.
- [9] L. Ward, A. Dunn, A. Faghaninia, N. E. R. Zimmermann, et al. Matminer: An open source toolkit for materials data mining. *Computational Materials Science*, 152:60–69, 2018.
- [10] N. Alampara, M. Schilling-Wilhelmi, and K. M. Jablonka. Lessons from the trenches on evaluating machine-learning systems in materials science. *Computational Materials Science*, 250:113391, 2025.
- [11] A. Jain, S. P. Ong, G. Hautier, et al. Commentary: The materials project: A materials genome approach to accelerating materials innovation. *APL Materials*, 1:011002, 2013.
- [12] P. H. Mott and C. M. Roland. Limits for poisson’s ratio in isotropic materials. *Physical Review B*, 80:224104, 2009.
- [13] G. Simmons and H. Wang. *Single Crystal Elastic Constants and Calculated Aggregate Properties*. MIT Press, Cambridge, MA, 1971.
- [14] T. Ouyang et al. Anomalous poisson’s ratio in two-dimensional materials. *Physical Review B*, 100:085425, 2019.
- [15] A. M. Maldonado, H. Tran, and A. Jain. Data-driven discovery of elastic properties of inorganic materials. *npj Computational Materials*, 6:143, 2020.
- [16] T. Hastie, R. Tibshirani, and J. Friedman. *The Elements of Statistical Learning: Data Mining, Inference, and Prediction*. Springer, New York, 2 edition, 2009.
- [17] S. M. Lundberg and S.-I. Lee. A unified approach to interpreting model predictions. In *Advances in Neural Information Processing Systems*, volume 30, pages 4765–4774, 2017.
- [18] C. R. Pidgeon. Band-structure and effective masses in semiconductors. In S. O. Kasap and P. Capper, editors, *Springer Handbook of Electronic and Photonic Materials*, chapter 5. Springer, Boston, MA, 2006.